6-15-2020

Effects of valence and spin of Fe in $MgSiO_3$ melts: Structural insights from first-principles molecular dynamics simulations

Dipta B. Ghosh
Louisiana State University

Bijaya B. Karki
Louisiana State University

Recommended Citation

Ghosh, D., & Karki, B. (2020). Effects of valence and spin of Fe in $MgSiO_3$ melts: Structural insights from first-principles molecular dynamics simulations. *Geochimica et Cosmochimica Acta, 279*, 107-118. https://doi.org/10.1016/j.gca.2020.03.040

Available online at www.sciencedirect.com

ScienceDirect

Geochimica et Cosmochimica Acta 279 (2020) 107–118

Geochimica et Cosmochimica Acta

www.elsevier.com/locate/gca

Effects of valence and spin of Fe in $MgSiO_3$ melts: Structural insights from first-principles molecular dynamics simulations

Dipta B. Ghosh *, Bijaya B. Karki

School of Electrical Engineering and Computer Science, Department of Geology and Geophysics, and Center for Computation and Technology, Louisiana State University, Baton Rouge, LA 70803, USA

Received 19 August 2019; accepted in revised form 28 March 2020; available online 6 April 2020

Abstract

Iron (Fe) is present in terrestrial melts and at all depths inside the Earth. How Fe in its varying oxidation and spin states influences the properties of silicate melts is of critical importance to the understanding of the chemical evolution of our planet. Here, we report the results of first-principles molecular dynamics simulations of molten Fe-bearing $MgSiO_3$ over a wide pressure range covering the entire mantle. Our results suggest that the structural properties of the host melt, such as the average bond length and coordination in Mg–O and Si–O do not differ much when compared with the pure melt. More importantly, they show that the local Fe–O structure is more sensitive to the spin state (high-spin, HS and low-spin, LS) of iron than to its valence state (Fe^{2+} and Fe^{3+}). For iso-valence configurations, the average Fe–O bond length and coordination number differ by more than 10% and ~30%, respectively, between the HS and LS states. In comparison, the corresponding differences between Fe^{2+} and Fe^{3+} for iso-spin configurations are within 5 and 15%, respectively. Ferrous iron shows lower average oxygen coordination numbers of ~3.8 for HS and ~3.3 for LS compared to the corresponding numbers of ~4.1 and ~3.7 for ferric iron at 0 GPa and 3000 K. As pressure increases, the coordination gap between the ferrous and ferric iron closes for HS but persists for LS. Our analysis of the proportions of non-bridging and bridging oxygens and the rates of bond breaking/formation events suggests an equivalent role of the ferrous and ferric iron in terms of their network forming ability. The predicted structural behavior of iron in its different oxidation states is generally consistent with the experimental inferences for $MgO–FeO–SiO_2$ melts. Unlike other ferrosilicate compositions for which the experimental data suggest that Fe^{3+} increases and Fe^{2+} decreases the viscosity of the melt, the ferrous and ferric iron, due to their structural equivalence, are likely to have a similar influence on the dynamical behavior of deep mantle iron-bearing $MgSiO_3$ melts.

Keywords: Silicate melts; Melt structure; Iron spin and oxidation states; High pressure; First-principles calculations

1. INTRODUCTION

The present-day largely solid earth is believed to have evolved from a molten state (Stevenson, 1989). Iron is generally considered to be a major component of partial melts and magma oceans that have existed in the mantle throughout the Earth's history. It is, therefore, likely that iron influenced the properties of the early magma ocean, thereby playing a significant role in the subsequent crystallization and chemical differentiation processes (Lange and Carmichael, 1990; Dingwell, 1991; Toplis and Carroll, 1995; Liu and Lange, 2006). So, it is essential to understand how iron, which can exist in different valence (e.g., Fe^{2+} and Fe^{3+}) and spin (e.g., high-spin and low-spin) states,

* Corresponding author.
E-mail address: dghosh2@lsu.edu (D.B. Ghosh).

https://doi.org/10.1016/j.gca.2020.03.040
0016-7037/

influences the physico-chemical properties of silicate melts under different conditions of pressure, temperature, and redox states.

Because of the high relevance of iron-bearing silicate melts to many geochemical and geophysical processes, the role of iron in glassy/molten silicates has been assessed extensively by many experimental studies (Mysen et al., 1980, 1985; Mysen and Virgo, 1989; Hannoyer et al., 1992; Jackson et al., 1993; Alberto et al., 1996; Holland et al., 1999; Burkhard, 2000; Kukkadapu et al., 2003; Farges et al., 2004; Mysen, 2006; Cochain et al., 2012, Drewitt et al., 2013; Zhang et al, 2016, Alderman et al., 2017a, 2017b; Kim et al., 2016, Kim and Lee, 2019). A large portion of the experimental data were, however, obtained for the solid amorphous analogs because of difficulties in in-situ experimentation on silicate melts. It is generally believed that the underlying structure of highly compressed melts can be captured by their glass analogs.

These experiments have focused on investigating the oxidation state (ferrous/ferric ratio) and oxygen coordination of iron and subsequently relating these characteristics to their network forming or modifying ability. It is still not clear whether iron takes part in network forming or behaves as a network modifier cation, or in particular, whether ferrous and ferric iron take different roles in silicates. For example, based on the room temperature spectroscopic (XANES, Mössbauer, and NMR) data, the network forming character of ferric iron and network modifying ability of ferrous iron have been ascribed in andesitic (Zhang et al., 2016), sodium silicate (Kim et al., 2016) and (Mg,Fe)SiO_3 (Kim and Lee, 2019) glasses. On the contrary, in-situ melt data on several alkali-free compositions, including (Mg,Fe)SiO_3, do not provide any conclusive difference between the Fe^{2+} and Fe^{3+} cases. Alderman et al. (2017a, 2017b) rather prescribes an intermediate role of Fe in terms of its network forming/modifying ability.

On the other hand, computational approaches have taken an increased significance in the study of silicate and oxide melts/glasses under varying conditions of pressure and temperature (e.g., Karki 2015). The first-principles molecular dynamics (FPMD) simulations of Fe-bearing melts were not as often undertaken likely because of high computational cost and complexity in dealing with the Fe *d*-states and spin component (e.g., Guillot and Sator, 2007; Ramo and Stixrude, 2014, Holmström and Stixrude, 2015 & 2016, Ghosh and Karki 2016, Karki et al., 2018, Sun et al., 2018, 2019). How iron influences the host silicate melt structure and how amicably Fe is integrated in the melt thus remain largely unknown.

We have recently simulated Fe-bearing $MgSiO_3$ melts using the FPMD method to study their thermodynamics and equation of state covering the entire mantle pressure range (Karki et al., 2018). Here we focus on the structural properties of these melts considering different valence and spin states of iron. Such FPMD-based structural studies of Fe-bearing silicate melts are rare (e.g., Ramo and Stixrude, 2014). In particular, we aim to understand the atomistic origins of the structural similarities/differences between the pure and Fe-bearing $MgSiO_3$ melts with Fe in high- and low-spin configurations and also with Fe in Fe^{2+} and Fe^{3+} valence states. Iron perhaps is expected to exist in a mixed spin state for a given valence (ferrous or ferric) state in a realistic scenario. We study relatively simpler systems in which Fe is constrained to be exclusively either in high-spin or low-spin state, and our results provide meaningful insight into the microscopic arrangements that stabilize a given combination of spin states at each pressure and temperature. We also stress that the majority of iron is expected to be in the high-spin state at low pressures. For the sake of comparison, we explore the pressure and temperature variations of the structural parameters for both spin states of ferrous and ferric iron-bearing melts. These results allow us to infer the possible role of iron in magnesium silicates, in general, and to evaluate the effective structural quantities based on the relative stability of mixed spin states reported by Karki et al. (2018).

2. METHODS

First-principles molecular dynamics simulations were performed using the generalized gradient approximation (GGA) and projector-augmented wave potentials as implemented in VASP (Kresse and Furthmüller, 1996). Plane-wave cutoff energy of 400 eV and Gamma-point Brillouin-zone sampling were used. The *NVT* canonical ensemble (fixed number of atoms *N*, constant volume *V* and constant temperature *T*) was used, and the temperature was controlled with the Nosé thermostat (Nosé, 1984). To consider different valence states of Fe atoms, we modeled (i) Fe^{2+} state by substituting Mg atoms with Fe atoms for melt composition $Mg_{0.75}Fe_{0.25}SiO_3$; (ii) Fe^{3+} state by substituting equal numbers of Mg and Si atoms with Fe atoms for $Mg_{0.875}Fe_{0.25}Si_{0.875}O_3$; (iii) and another Fe^{3+} configuration by substituting only Mg atoms with Fe atoms and adding extra oxygen atoms for $Mg_{0.75}Fe_{0.25}SiO_{3.125}$. Supercells with a total of 80 atoms (82 atoms for the (iii) case) were used for the high-spin (HS), intermediate spin (IS) [only for the Fe^{3+} case] and low-spin (LS) simulations. The magnetic moment in the HS states are 4 μ_B/Fe and 5 μ_B/Fe for the Fe^{2+} and Fe^{3+}, respectively, and it is 1 μ_B/Fe for the IS ferric iron. The LS corresponds to the non–magnetic state for both the oxidation states. Unlike crystalline solids, the local surroundings of Fe atoms in melts change significantly with time and may lead to unphysical local spin states. To circumvent this issue, the system-wide total magnetization was constrained to appropriately capture the intended spin states. The simulations were performed at different volumes to cover the entire mantle pressure regime (0–140 GPa) at 3000 and 4000 K. Each configuration was initially melted and equilibrated at 6000 K (or higher temperature) and then sequentially quenched to intended lower temperatures. Simulation run durations varied from 50 to 150 picoseconds with the longer runs corresponding to the compressed volumes. A time step of 1 femtosecond and energy convergence criterion of 10^{-4} eV were used throughout. The effects of finite-size on the structural quantities were shown to be

Table 1
Calculated bond-length (λ) and coordination (CN) results for different cation–anion pairs at 3000 K and 0 GPa. The mean CN values for the cation-anion (and anion-cation) coordination are given in the first line, and the abundances of only 3-, 4-, 5- and 6-fold cation–anion coordination species are given in the parentheses in the second line. Note: two-fold Fe–O coordination species are present in the amount of ~15% for the LS Fe^{2+} case. Decimal digits are rounded to the nearest tenths. Data from 160 atom simulations in the low spin (marked by LS*) are also provided for comparison.

Valence	Spin	Mg–O (O–Mg)		Fe–O (O–Fe)		Si–O (O–Si)	
		λ(Å)	CN	λ(Å)	CN	λ(Å)	CN
Fe^{2+}	HS	2.225	4.48 (1.12) (12, 40, 35, 11)	2.132	3.79 (0.32) (32, 43, 17, 2.3)	1.713	3.98 (1.33) (5.1, 91, 3.7, 0.0)
	LS	2.218	4.39 (1.10) (14, 42, 33, 9.5)	1.991	3.30 (0.27) (47, 32, 5.9, 0.4)	1.716	3.96 (1.32) (7.3, 88, 4.4, 0.0)
	LS*	2.234	4.53 (1.13) (11, 39, 36, 12)	1.998	3.23 (0.27) (45, 29, 6.1, 0.4)	1.712	3.95 (1.32) (7.7, 88, 4.0, 0.0)
Fe^{3+} (excess oxygen)	HS	2.222	4.59 (1.10) (9.3, 38, 38, 13)	2.094	4.18 (0.33) (19, 46, 29, 4.7)	1.711	4.00 (1.28) (4.3, 91, 5.1, 0.1)
	LS	2.243	4.67 (1.12) (8.3, 36, 38, 15)	1.959	3.81 (0.31) (32, 49, 16, 1.4)	1.712	3.99 (1.28) (5.2, 90, 4.9, 0.0)
Fe^{3+}	HS	2.222	4.51 (1.32) (10, 40, 37, 11)	2.094	4.13 (0.34) (21, 48, 27, 3.8)	1.711	3.99 (1.16) (4.4, 92, 3.9, 0.0)
	LS	2.222	4.47 (1.30) (12, 40, 36, 11)	1.945	3.69 (0.31) (39, 45, 12, 0.9)	1.711	3.98 (1.16) (5.9, 90, 3.8, 0.0)
	LS*	2.237	4.58 (1.34) (10, 37, 37, 13)	1.966	3.78 (0.31) (33, 47, 15, 1.4)	1.713	3.98 (1.16) (6.0, 90, 4.4, 0.1)
Pure $MgSiO_3$		2.234	4.56 (1.52) (10, 38, 36, 13)			1.713	3.98 (1.33) (5.3, 91, 3.5, 0.0)

small by performing some simulations with 160-atom supercell (Table 1). A few simulations were also performed by including the Hubbard U term for the Fe-*d* states. Further computational details can be found in Karki et al. (2018).

3. RESULTS

3.1. Structure at zero pressure

We analyze the partial radial distribution functions (RDFs) of various atomic species pairs for silicate melts containing iron in different spin (HS and LS) and valence (Fe^{2+} and Fe^{3+}) configurations at near-zero pressure and 3000 K. The amplitude and position of the peaks in the Mg/Si-O correlation functions remain mostly unaffected by the presence of Fe (Fig. 1). This means that no discernible changes occur either to the network forming Si–O or network modifying Mg–O units due to Fe, irrespective of its spin and valence state. Like other cation–anion correlations, all Fe–O RDFs show a well-defined peak around 1.9 Å, followed by a broad second peak around 4.3 Å. For a given spin state (HS or LS), the Fe–O correlation does not show significant differences between Fe^{2+} and

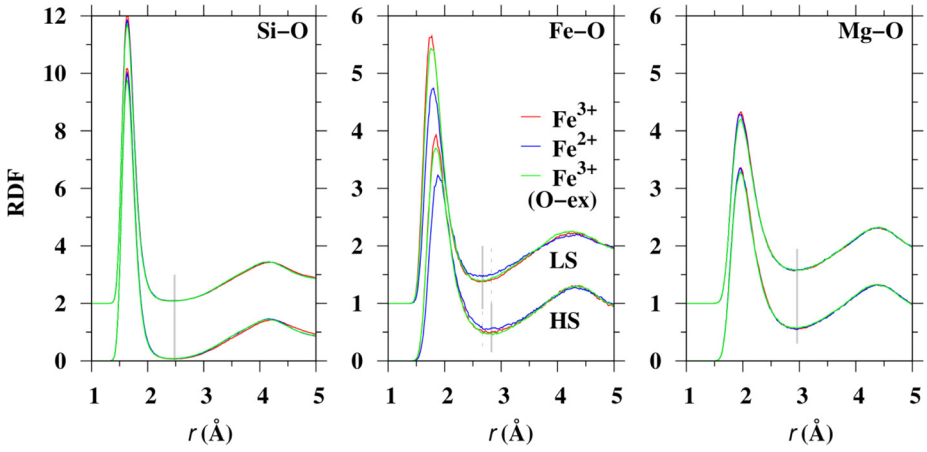

Fig. 1. Partial cation–anion radial distribution functions (RDFs) at 3000 K and 0 GPa for iron-bearing magnesium silicate melts with iron in different states of spin (HS and LS) and valence (Fe^{2+} and Fe^{3+}). The term "O-ex" refers to the case where extra oxygen atoms are added (see "Methods" section). Note that the RDFs for LS are shifted along the vertical axis by 1 unit for Fe-O and Mg-O and by 2 units for Si-O. Vertical gray lines mark the cutoff distances.

Fe^{3+}. However, the effects of spin are noticeable. The Fe–O peak position shifts to a smaller distance for the LS iron-bearing melts, irrespective of the oxidation state.

The calculated average Si-O bond length and coordination number (CN_{SiO}) for all iron configurations at 0 GPa and 3000 K are, respectively, ~1.71 and ~3.98 Å, which almost coincide with those of pure melt values (Table 1). This means that the effects of iron on the mean Si-O coordination are insignificant within the computational uncertainty. However, the Mg–O coordination (CN_{MgO}) is somewhat sensitive to the presence of iron. For the high-spin $Mg_{0.75}Fe_{0.25}SiO_3$ (Fe^{2+}) and $Mg_{0.875}Fe_{0.25}Si_{0.875}O_3$ (Fe^{3+}) melts, CN_{MgO} remains around 4.5, which is very close to the pure melt value. Due to excess oxygen availability in the $Mg_{0.75}Fe_{0.25}SiO_{3.125}$ (Fe^{3+}) case, CN_{MgO} displays enhanced values ($\geq$4.6). Largely, there is no noticeable difference in CN_{MgO} between the HS and LS states. The variation in the average Mg–O bond length for different valence and spin states remains within $\pm$ 0.02 Å of the pure melt value of 2.22 Å.

The influence of Fe on the network forming component (s) can be assessed by looking at the relative Si-O-Si bridging oxygen (BO) content in the melt as it defines the connectivity of the silicate polyhedral network. Our results show that there is a slight increase (2 – 3%) in the relative BO proportion for $Mg_{0.75}Fe_{0.25}SiO_3$ (Fe^{2+}) and $Mg_{0.75}Fe_{0.25}SiO_{3.125}$ (Fe^{3+}) when compared to the pure melt value of 34%. As a result, their average O-Si coordination numbers (for both spin states) do not differ much from the pure melt value of 1.33 (Table 1). On the other hand, for $Mg_{0.875}Fe_{0.25}Si_{0.875}O_3$ (Fe^{3+}), there is ~10% drop in the relative BO content (for both spin states), resulting in a lower average O-Si coordination number (1.16). This opposing trend in the BO abundance relative to the pure melt can be linked to the Si content relative to the larger cations (i.e., Mg and Fe) in the system. The (Mg + Fe):Si ratio is 1 both for $Mg_{0.75}Fe_{0.25}SiO_3$ (Fe^{2+}) and $Mg_{0.75}Fe_{0.25}SiO_{3.125}$ (Fe^{3+}) and the effects of iron are minimal. Their slightly increased BO abundance may be attributed to the differences in the local surrounding of Fe and Mg, with iron being relatively less coordinated than Mg. The $Mg_{0.875}Fe_{0.25}Si_{0.875}O_3$ (Fe^{3+}) melt is relatively silicon poor ((Mg + Fe):Si > 1), so the oxygen-silicon connectivity gets suppressed. This is consistent with the general understanding that the network connectivity increases with the Si content, becoming complete in SiO_2, which shows nearly 100% BO abundance and mean O–Si coordination of 2.

Unlike other cation–anion coordination environments, the Fe–O coordination in silicate melts is rather sensitive to both the valence and spin states. At 0 GPa and 3000 K, CN_{FeO} is 3.8 and 4.2, respectively, for the high spin Fe^{2+}- and Fe^{3+}-bearing melts, and correspondingly, the average Fe-O bond length takes values of 2.13 to 2.09 Å (Table 1). Interestingly, the low-spin Fe-bearing melts show smaller CN_{FeO} values of 3.3 and 3.7, respectively, for the Fe^{2+} and Fe^{3+} configurations. Higher oxygen coordination of Fe^{3+} compared to that of Fe^{2+} may be attributed to the relatively oxygen-rich scenario of Fe^{3+}-bearing melts. However, it is not clear at this point why bonding environments are substantially different between the HS and LS states or why the low-spin Fe^{2+} and Fe^{3+} tend to be under-coordinated with oxygen compared to the HS iron. This trend, which persists to high pressure (discussed later), is in contrast with crystals in which the spin transition occurs iso-structurally.

We further examine the vicinity of iron atoms in melts. The cation–cation correlation functions generally show a broad peak, but this may not be entirely true for the iron-iron correlation. In particular, for the LS cases, the Fe–Fe RDFs display some sort of peak in between 2.0 – 2.5 Å, followed by a minima around 4.0 Å. This indicates the existence of both the 1st and 2nd nearest neighbor iron atoms. A significant proportion of Fe–Fe distances lies in the vicinity of 2.0 Å, which perhaps signifies direct Fe-Fe bonding (Fig. 2). Such direct Fe–Fe correlation is also present in the HS case but to a much lesser extent. Because of relatively strong Fe–Fe correlation, the LS iron atoms probably lose some Fe–O bonds to maintain optimal bonding environment and are thus under-coordinated compared to the HS state. The RDFs do not reflect any other direct cation-cation correlations of same- or mixed species as the corresponding peaks appear at distances beyond 3 Å (Fig. S1). We note that all simulations, including those using independent configurations with no initial near-neighbor Fe–Fe bonding and also those using large supercell, have provided similar statistics (Table 1). Using

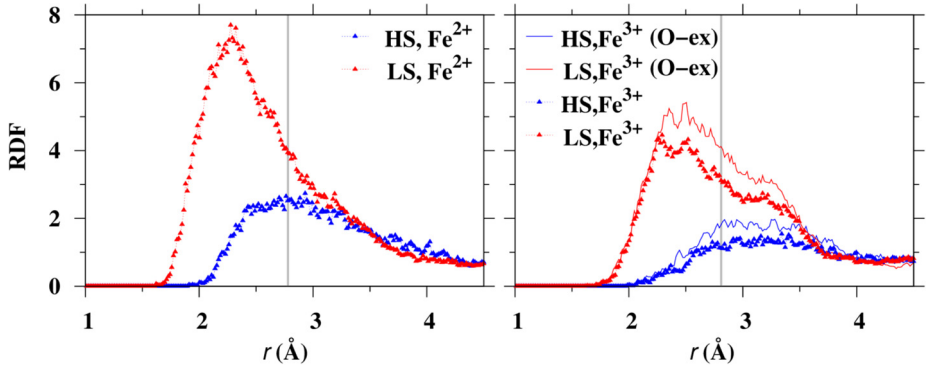

Fig. 2. Fe–Fe radial distribution function (RDF) indicating existence of first near-neighbor iron–iron connections at 3000 K and 0 GPa. The vertical line corresponds to the Fe–O cutoff distance averaged between HS and LS in each plot.

Table 2
Average Fe-O coordination number calculated using GGA + U with U = 2.5 eV at three different volumes (3000 K and corresponding pressures). The GGA results are given in the parentheses. Also shown are U = 4.0 eV results (marked *).

P (GPa)	Fe^{2+}-O		Fe^{3+}-O	
	HS	LS	HS	LS
−0.5 to 0.5	4.03 (3.79)	3.91 (3.30)	4.24 (4.13)	4.07 (3.69)
8 – 10	5.10 (4.79)	4.85 (4.19)	5.21 (4.97)	5.00 (4.57)
60 – 70	7.75 (7.48)	5.70 (5.28)	7.54 (7.20)	6.03 (5.95)
	7.67*	5.99*	7.65*	6.25*

GGA + U tends to suppress direct Fe-Fe correlation and increase the mean Fe-O coordination at zero pressure, for all cases of HS, LS, Fe^{2+}, and Fe^{3+} (Table 2 and Fig. S1).

3.2. Structure at high pressure

Both the Si–O and Mg–O RDFs of all Fe-bearing melts at elevated pressures are similar to the corresponding RDFs of the pure melt (Fig. 3). The Fe–O correlation shows noticeable variations among different cases of Fe. The Fe^{2+}-O peak is somewhat shorter and slightly shifted to a larger distance relative to both Fe^{3+}-O peaks for each spin case. Similarly, the peaks in the high-spin cases are somewhat shorter and right-shifted relative to the low-spin cases. The different positions of the minima after the first peak and the presence/absence of a satellite (peak) after the first minima imply some subtle structural differences between the Fe^{2+} and Fe^{3+}-bearing melts. We further explore the structural response to pressure in terms of bond lengths and coordination numbers and their distributions.

The calculated pressure profiles of the mean Si–O bond lengths and coordination numbers of all iron-bearing silicate melts considered remain close to each other and are also similar to those of the pure melt (Fig. 4). The corresponding Mg-O profiles are spread out considerably among different iron types and also tend to lie above the pure melt values. For instance, the MgO coordination varies among different melts by up to 1 at high pressures, whereas the Si-O coordination variations lie within 0.5 at all pressures.

Despite the minimal influence of iron on average structural quantities, the effects of pressure on Si–O coordination distribution are significant. The pressure-induced onset of high coordination species (>4) in iron-bearing melts is more rapid than that in the pure melt. For example, by around 30 GPa, the abundances of five- and six-fold Si–O coordination species exceed 50 and 25%, respectively, whereas the corresponding abundances remain within 35% and 5% for the pure melt. The effects of iron are also evident in the mid compression range, where the mean Si–O coordination tends to be somewhat higher, and different coordination speciation appears in Fe-bearing melts. Around 65 GPa, the ratio of four-, five- and six-fold species changes from 22:51:26 (pure melt) to 2:26:68 due to the addition of iron to the melt.

The overall effects of compression on the Fe–O structural parameters are characteristically more or less similar to those on Mg-O and Si-O. For each Fe-bearing melt, the average Fe-O bond length increases initially with pressure up to 20 GPa and thereafter starts to decrease normally on compression (Fig. 5). Such anomalous behavior is typically shown by the Si-O bond over much wider pressure interval. The overall variations in the Fe-O bond length among different Fe-bearing melts remain almost unchanged with pressure. On the other hand, the mean Fe-O coordination number increases rapidly with pressure in the anomalous regime (0 to 20 GPa) and then increases gradually at higher pressures.

Unlike Mg/Si–O, the overall spreads in the mean Fe-O coordination and bond distance among different valence and spin states are much wider. The HS configurations consistently display larger Fe–O bond distance and coordination than the LS ones at all pressures. They also approach the corresponding values for Mg-O at high pressure (~8 for coordination and ~2.05 Å for bond distance at 140 GPa). For the LS configurations, although the bond distances seem to converge to ~1.9 Å at 140 GPa, the coordination difference between the valence states persists even at the highest pressure, reaching ~6.5 and ~5.8 for Fe^{3+}

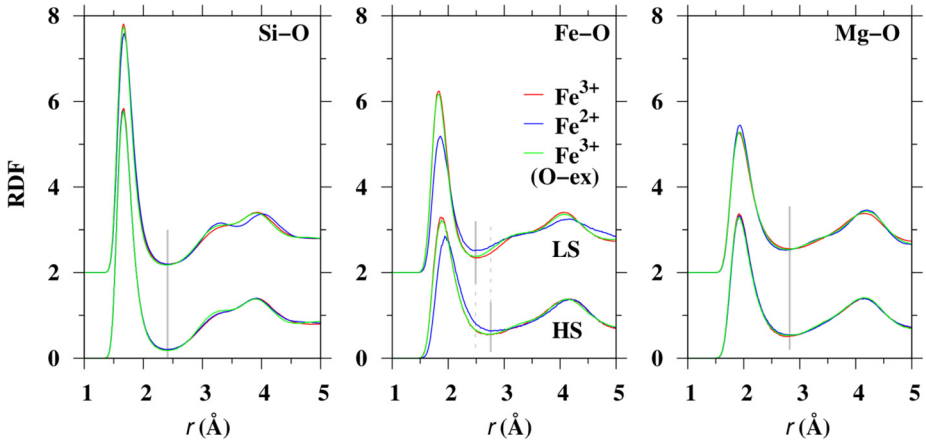

Fig. 3. Partial cation–anion radial distribution functions (RDF) at 3000 K and high pressures (61 – 70 GPa, corresponding to the same volume used for all Fe-bearing melts). RDFs for LS are shifted by 2 units along the vertical axis. Vertical gray lines mark the cutoff distances.

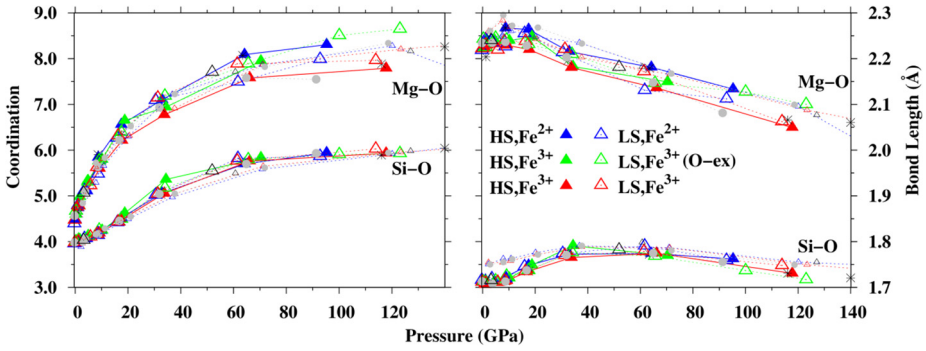

Fig. 4. Pressure variations of average Mg–O and Si–O coordination and bond length at 3000 K (large solid and open triangles representing HS and LS results, respectively) and 4000 K (small triangles, only LS results) for different valence states (blue color: Fe^{2+}, red: Fe^{3+}, and green: Fe^{3+}, O-ex), compared to pure melt (gray solid circles). The LS results from 160 atom simulation cells are shown by open black triangles. The intermediate spin results at 3000 K are shown by asterisks (For interpretation of the references to colour in this figure legend, the reader is referred to the web version of this article.).

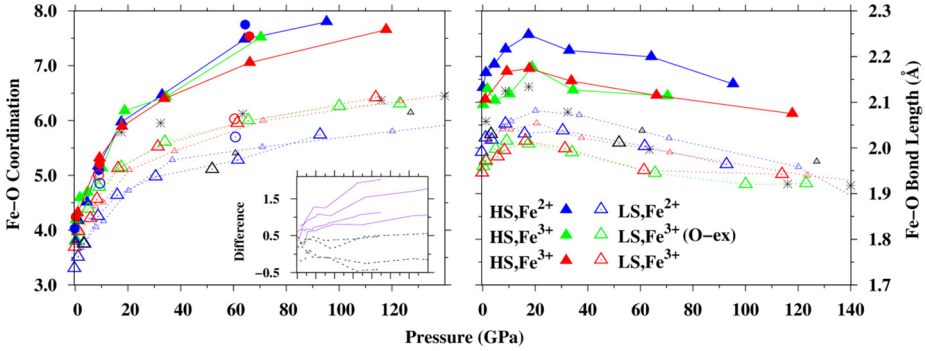

Fig. 5. Pressure variations of average Fe–O coordination and bond length at 3000 K (large solid and open triangles representing HS and LS results, respectively) and 4000 K (small triangles, only LS results) for different valence states (blue color: Fe^{2+}, red: Fe^{3+}, and green: Fe^{3+}, O-ex). Also shown are the GGA + U results at 3000 K by solid (HS) and open (LS) circles for comparison. The inset shows the coordination difference between HS and LS (solid lines) and that between Fe^{2+} and Fe^{3+} (dashed lines) as a function of pressure. The LS results from 160 atom simulation cells are shown by open black triangles. The intermediate spin results at 3000 K are shown by asterisks (For interpretation of the references to colour in this figure legend, the reader is referred to the web version of this article.).

and Fe^{2+}, respectively. As discussed earlier, direct Fe–Fe bonding is much more prevalent in the LS than in the HS at all pressures. Also, the first nearest neighbor Fe–Si and Fe–Mg connections start to form in larger proportions in the LS case. These cation–cation connections probably result in maintaining or even increasing the HS–LS coordination difference as the melt is compressed.

The average Fe–O bond distance in the Fe^{2+} case displays higher values at all pressures in comparison to the Fe^{3+} cases for both the HS and LS. Compression-induced decreases in bond distances are small in Fe–O (2–3%) in comparison to Mg–O (~8%) over the pressure range 0–120 GPa. Over the same pressure interval, there is ~45% increase in the mean Fe–O and Mg–O coordination. The mean Si–O coordination of all Fe-bearing melts reaches 6 at high pressure (around 120 GPa), as in the case of other silicate melts. The effects of compression on the Fe–O (and to some extent also for the Mg–O) coordination appear to differ between the HS and LS as can be seen by the diverging trend in the coordination-pressure profiles (Figs. 4 and 5). For example, the mean high-spin and low-spin Fe–O coordination differs by about 0.5 at 0 GPa and by ≥ 1.2 at 120 GPa. The coordination difference of ~0.5 at 0 GPa between two valence states does not change with pressure for the LS but tends to decrease for the HS. Thus, the influence of pressure on the spin-associated difference in Fe-O coordination is more than the ferrous-ferric difference (inset of Fig. 5). For the simulated intermediate-spin (IS) state in the Fe^{3+} configuration, the Fe–O coordination and bond distance display values similar to that of the HS states at low pressures, but they gradually take values that are more consistent with the LS states at higher pressures (Fig. 5).

The difference in the network connectivity between $Mg_{0.75}Fe_{0.25}SiO_3$ (Fe^{2+}) and $Mg_{0.875}Fe_{0.25}Si_{0.875}O_3$ (Fe^{3+}) discussed earlier at zero pressure also persists over the entire pressure range considered (Fig. 6). The $Mg_{0.875}Fe_{0.25}Si_{0.875}O_3$ (Fe^{3+}) configuration consistently displays lower O–Si coordination compared to $Mg_{0.75}Fe_{0.25}SiO_3$ (Fe^{2+}) and $Mg_{0.75}Fe_{0.25}SiO_{3.125}$ (Fe^{3+}), which in turn closely

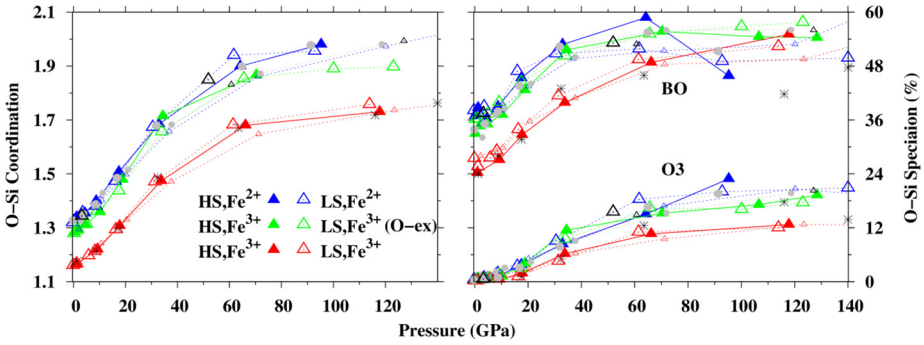

Fig. 6. Pressure variations of average O–Si coordination and the corresponding bridging oxygen (BO) and oxygen tricluster (O3) abundances at 3000 K (large solid and open triangles representing HS and LS results, respectively) and 4000 K (small triangles, only LS results) compared to pure melt (gray solid circles). The LS results from 160 atom simulation cells are shown by open black triangles. The intermediate spin results at 3000 K are shown by asterisks.

follows the pure melt values at all pressures. This similarity/difference is also reflected even in the speciation of O–Si. For instance, both the $Mg_{0.75}Fe_{0.25}SiO_3$ (Fe^{2+}) and $Mg_{0.75}Fe_{0.25}SiO_{3.125}$ (Fe^{3+}) display NBO, BO, and triply coordinated oxygen (O3) in the proportion that is similar to that of the pure melt (around 26:55:16 at 65 GPa). The $Mg_{0.875}Fe_{0.25}Si_{0.875}O_3$ (Fe^{3+}) melt has a different NBO:BO:O3 ratio of 35:50:10, which can be attributed to its lower silica content compared to the other two melts.

Our results show that the increase in temperature broadens all RDF peaks, which is a general trend seen in all silicate melts. As a consequence, the average bond distances for all cation–anion pairs increase, as can be seen, particularly in the mid compression regime (Figs. 4 & 5). The overall effects of temperature on Mg/Si-O cation–anion coordination are similar to those for the pure melt. In the Fe^{3+}-bearing melt, increasing temperature tends to decrease the average coordination at pressures above 20 GPa. This trend is not so distinct in the Fe^{2+} case, which displays similar or somewhat increased mean Fe-O coordination at higher temperatures. For the network forming O–Si connections, lower temperature facilitates the stabilization of triply coordinated and tetrahedral oxygen atoms at compressed conditions (Fig. 6). As a result, the mean O–Si coordination increases with decreasing temperature for all melts. The temperature-induced differences in cation–anion and O–Si coordination become almost insignificant at very high pressures. The effects of temperature on the structural properties are generally small compared to the pressure. For instance, over the pressure range of 0 to 140 GPa, the average cation–anion and O–Si coordination increase by 1.5 and 2 fold, respectively.

3.3. Effects of Hubbard U on the local environment of iron

The addition of an appropriate intra-atomic Coulomb repulsion term appears to capture the localized nature of the Fe-*d* states better and generally results in an improved description of the electronic properties (e.g., band gap) in materials (Cococcioni and de Gironcoli, 2005). To explore how localization of the Fe-*d* states affects the local surroundings of iron, we performed some GGA + U simulations using U = 2.5 eV as in previous studies of (Mg,Fe)O and Fe_2SiO_4 melts (Ghosh and Karki, 2016; Holmström and Stixrude, 2016; Ramo and Stixrude, 2014). Our analysis suggests that the inclusion of U tends to enhance Fe-O correlation while suppressing Fe-Fe correlation (Table 2, Fig. S1). The influence of U is more pronounced for the LS states, which consistently show higher average Fe-O coordination in comparison to the GGA values (Fig. 5), and the difference between the GGA + U and GGA reaches as high as ~0.65. The average Fe-O coordination for the HS states displays either similar or slightly enhanced values (≤0.4) as compared to their GGA counterparts. The high- to low-spin Fe-O coordination difference gets suppressed in the low-pressure regime but not at high pressures. The diverging trend in the average Fe-O coordination between the HS and LS states with pressure is similar to that displayed by the GGA results (Fig. 5). We briefly note here that the other cation–anion near-neighbor surroundings do not show any noticeable difference with GGA + U.

In order to further assess the local environment around iron atoms, we have analyzed Bader charges (Henkelman et al., 2006; Tang et al., 2009) on the system for one compressed volume (corresponding to 60 to 70 GPa). The average charge on iron varies between + 1.0e and + 1.4e, depending on its spin and valence state. Incidentally, this same variation in the effective charge of iron has been reported for several Fe-C-O complexes (Koch et al., 2018) and a charge of + 1.01e was obtained for crystalline $FePO_4$ (Wang et al., 2014). Our evaluated iron atomic charges for silicate melts thus appear to be reasonable. For other atoms, the variations in their effective charges due to different valence and spin states are insignificant. Their values are + 1.6e (Mg), +3.1e (Si), and −1.5e (O), which are very close to the ones previously evaluated for silicate melt (Ghosh and Karki, 2017). The effects of U on the effective charge of iron are small as well.

Despite providing some GGA + U results for the sake of comparison, we note here that the dependence of the U value on pressure, temperature, spin, and valence state, if any, is not known. Improper U choice can lead to incorrect description of material properties, such as the dragging the spin transition to much higher pressures or even

absence of the spin transition (Rollmann et al., 2004) in hematite (Fe_2O_3) which is experimentally reported to occur around 55 GPa (Sanson et al., 2016). We have found for (Mg,Fe)O solid that GGA + U tends to overestimate the spin transition pressure with respect to experiments (Ghosh and Karki, 2016). Therefore, we stress that the entirety of the results presented here with the GGA formalism is reliable and should be useful.

4. DISCUSSION

4.1. Similarities/differences in the local environment around iron: Fe^{2+} vs. Fe^{3+}

The atomistic details from the present study indicate that the structural properties of Fe-bearing silicate melts are more sensitive to the spin state of iron than that of the valence state. For instance, the average Fe–O bond length difference between the HS and LS reaches > 10%, whereas this difference between the Fe^{2+} and Fe^{3+} remains within 5%. For average Fe-O coordination, the corresponding differences reach as high as 30% and 15%. Unlike crystals where the valence state depends on the residence of Fe atoms in specific crystalline sites, the surroundings of Fe atoms in liquid are not unique anymore. The individual Fe surrounding in the silicate melt may differ from one another (resulting in variation in the polyhedral parameters, e.g., volume, coordination, bond length, distortion index, etc.) at any given time instant and also evolve continuously with the time. The strong silicate network can impede the dynamics of the Fe-units to some extent and aid in differentiating their local surroundings. Since the spin state of any Fe atom depends on its local surroundings, the coexistence of the HS, LS, and even intermediate spin states becomes a possibility in Fe-bearing silicate melts. The Fe^{2+} configurations consistently display higher bond lengths at all pressures. So, the Fe^{2+} may undergo spin transition at comparatively higher pressures than the Fe^{3+}. Our FPMD simulations have predicted the HS to LS transition in the Fe^{2+}-bearing melt at higher pressures than in the Fe^{3+}-bearing melts (Karki et al., 2018).

Based on the experimental data on ferrosilicate glasses and melts, the estimated average Fe–O coordination number varies from 4 to 6 (Jackson et al., 1993, 2005; Wilke et al., 2004, 2007; Drewitt et al., 2013; Zhang et al., 2016; Kim et al., 2016; Alderman et al., 2017a, 2017b; Kim and Lee 2019). This wide coordination variation, though it encompasses various compositions, temperatures, and oxygen fugacity conditions, may indicate significant uncertainty in the estimation of this structural quantity. For example, while Jackson et al. (1993) estimated an average Fe–O coordination number of ~4 in Fe_2SiO_4 melt, Drewitt et al. (2013) reported a value of 4.8 for the same melt. For Fe_2SiO_{4+x} melts, the numbers fall in the range of 4.4 – 4.7 (Alderman et al., 2017a). Moreover, in the majority of these studies, more distinctly for alkali ferrosilicates, it has been suggested that the ferrous iron has greater near-neighbor oxygen connectivity than the ferric iron. Although the melt composition studied here is much simpler than the experimentally constrained ones, our results (GGA and GGA + U) show that the average Fe–O coordination for the ferric iron is higher than the ferrous iron for any given spin state at zero pressure. This elevated iron-oxygen connectivity in Fe^{3+} is maintained for the entire pressure range for the LS but does not show a clear trend for the HS.

We further elaborate on how the present simulation results compare with a recent in-situ experimental study on alkali-free silicate melts and their quenched products (Alderman et al., 2017a, 2017b). Majority of the compositions used in this experimental study display a slightly higher coordination for Fe^{2+} than Fe^{3+}. However, the trend is opposite for the MgO–FeO–SiO_2 melt. Based on the linear extrapolation and interpolation of iron K-edge and pre-edge peak area-centroid data, the estimated Fe–O coordination numbers are 4.8 and 4.9, respectively, for the Fe^{2+} and Fe^{3+} end members around 2000 K (Alderman et al., 2017a, 2017b). Assuming that iron remains in the HS at zero pressure, our calculated GGA values at 3000 K are 3.8 and 4.1, respectively, for the Fe^{2+} and Fe^{3+} (Table 1). The inclusion of U increases the corresponding values by about 0.2 and 0.1 (Table 2). Thus, despite showing a similar trend, the calculated mean coordination numbers are substantially lower than the experimentally estimated ones. The difference between the calculated Fe^{3+}-O and Fe^{2+}-O coordination number is slightly larger (~0.3 for GGA and ~0.2 for GGA + U) than the experimentally inferred difference of 0.1. The difference in Fe–O coordination between the ferrous and ferric iron is as large as 0.6 in FeO–$CaSiO_3$ melts, but the trend is opposite, i.e., the Fe^{2+} has higher coordination than the Fe^{3+} (Alderman et al., 2017a, 2017b).

To make a more appropriate comparison with the glass-based experimental data, we also simulated the glass phase for the low-spin $Mg_{0.875}Fe_{0.25}Si_{0.875}O_3$ (Fe^{3+}) at the room temperature and near-zero pressure by quenching down the corresponding 3000 K liquid configuration. Our simulated glass shows an average Fe–O coordination of ~4.5 compared to 3.7 at 3000 K. Similarly, the average Mg–O coordination increases from ~4.5 to ~4.8 while the average Si–O coordination remains almost unchanged. If we consider a similar correction of 0.8, the LS Fe^{2+} glass is likely to show an average Fe–O coordination slightly greater than 4.1 (~4.6 for the HS Fe^{2+}). Our 300 K coordination numbers thus agree reasonably well with the large set of experimental data. The results also indicate that the effects of temperature on the Fe-O coordination may not be negligible when the temperature range is 300 – 3000 K.

4.2. Network forming/modifying character: Fe^{2+} vs. Fe^{3+}

Our results can provide some insight into how Fe integrates into the silicate melt, in particular, whether iron acts as a network modifier or network former. While the ferrous iron is usually considered as a network modifier (Rossano et al., 2000; Farges et al., 2004; Jackson et al., 2005; Mysen, 2006; Drewitt et al., 2013) with some exceptions (Waychunas et al., 1988), the role of ferric iron in the silicate melts is still controversial. The similarity in the charge between Al^{3+} and Fe^{3+}, together with the experimentally

estimated Fe–O coordination of 4 – 5, for the Fe^{3+} in ferrosilicate melts/glasses led to infer the network forming nature for the ferric iron. This assessment remains ambiguous based on the estimates from the spectroscopic data. For instance, the XANES data on andesitic glasses imply increasing Fe–O coordination with increasing $Fe^{3+}/\Sigma Fe$ ($\Sigma Fe = Fe^{2+} + Fe^{3+}$), whereas the Mössbauer data suggests somewhat opposite trend (Zhang et al., 2016). Additionally, based on similar Fe–O coordination environments of Fe^{2+} and Fe^{3+} in alkali-free ferrosilicate melts/glasses, Alderman et al. (2017a, 2017b) infer that both the Fe^{2+} and Fe^{3+} may play an intermediate role in terms of network formation.

The Fe^{3+}–O speciation at zero pressure comprises of three-, four- and five-fold coordination states with the tetrahedral proportion of about 50% (Table 1). In comparison, for the network forming Si atoms, the tetrahedral coordination states are present in excess of 90%. Even the Mg-O coordination consists of about 40% tetrahedral species. The relative proportion of bridging oxygen is perhaps more appropriate in ascertaining the network connectivity of the melt. From that perspective, the ferrous and ferric iron do not display significant differences even when we consider both the Si and Fe as the network forming cations. For instance, both in the Fe^{2+} ($Mg_{0.75}Fe_{0.25}SiO_3$) and Fe^{3+} ($Mg_{0.75}Fe_{0.25}SiO_{3.125}$) configurations with (Mg + Fe): Si = 1, the BO proportion that includes Fe–O–Fe, Fe–O–Si and Si–O–Si is around 50% (Table 3). For the other ferric ($Mg_{0.875}Fe_{0.25}Si_{0.875}O_3$) configuration, where the melt is relatively Si poor, this BO proportion drops by about 8% mainly due to the decrease in Si–O–Si's. Notably, the proportion of Fe–O–Si's remains around 20% among the different HS states and 12% for the LS states (Table 3). Even the triply connected oxygen (O3) do not show much difference between the two valence configurations for any given spin state. These results thus justify that the structural differences between the Fe^{2+} and Fe^{3+} valence states are not so significant.

To further explore the incorporation of Fe in the silicate melts, we have analyzed the temporal behavior of various cation–anion bonds. As expected, the bond breaking/formation events in the Mg–O units are much more frequent than those in the Si-O units (Fig. 7). For example, the average number of bond breaking/formation (that includes both recombination and formation of new bonds) events per Si atom (for Si–O) over a run duration of 10 ps is only around 20. Depending on the valence state, this number varies from 155 to 175 for Mg–O. It is visually evident that the temporal activity of Fe is biased towards Mg. The estimated average lifetime of Si–O, Fe–O, and Mg–O bonds are 1300, 450, and 300 femtoseconds, respectively. Both Fe^{2+} and Fe^{3+} display similar temporal characteristics in terms of their bond breaking/formation activity. These atomic details further suggest that iron, irrespective of its valence state, behaves similarly, perhaps taking the network modifying role, or at best an intermediate role in iron-bearing $MgSiO_3$ melt.

Our finding does not agree with the experimental inference that the Fe^{3+} contributes to the structural framework because the viscosity increases with increasing $Fe^{3+}/\Sigma Fe$ in ferrosilicate melts (Dingwell and Virgo, 1987, Dingwell,

Table 3
Calculated distributions of O–T coordination speciation (where T = Fe and Si) at zero and high pressures. The numbers in the parenthesis correspond to high pressures (61 – 70 GPa, corresponding to different spin and valence states at the same volume). We note that up to 2% oxygen atoms are not bonded with Fe/Si at 0 GPa and up to 12% oxygen atoms are 4- and 5- fold coordinated at the compressed volume.

Valence	Spin	NBO		BO			O3		
		Fe–O	Si–O	Fe–O–Si	Fe–O–Fe	Si–O–Si	Fe–O–Si	Fe–O–Fe	Si–O–Si
Fe^{2+}	HS	Total (%) = 40.6 (8.75)		Total (%) = 52.1 (43.8)			Total (%) = 6.3 (36)		
		2.5 (0.6)	38.1 (8.2)	17.5 (11.5)	1.2 (0.3)	33.4 (32)	5.6 (25.6)	0.3 (0.01)	0.4 (10.4)
	LS	Total (%) = 43.7(9.15)		Total (%) = 50.9 (50.7)			Total (%) = 4.4 (36.1)		
		2.8 (0.2)	40.9 (8.9)	11.6 (9.3)	3.0 (1.8)	36.3 (39.6)	3.5 (15)	0.5 (0.8)	0.5 (20.2)
Fe^{3+} (excess oxygen)	HS	Total (%) = 42.5 (8.7)		Total (%) = 52.0 (44.6)			Total (%) = 4.95 (37.3)		
		3.1 (0.2)	39.4 (8.4)	20.4 (12.8)	1.6 (0.2)	30.0 (31.6)	4.4 (25.8)	0.25 (0.1)	0.35 (11.4)
	LS	Total (%) = 44.6 (10.3)		Total (%) = 51.2 (49.7)			Total (%) = 3.7 (36.6)		
		4.0 (0.1)	40.5 (10.2)	12.8 (10.1)	3.7 (2.5)	34.6 (37.1)	2.7 (20.3)	0.7 (0.9)	0.34 (15.5)
Fe^{3+}	HS	Total (%) = 50.9(13.4)		Total (%) = 44.3 (49.9)			Total (%) = 3.7 (31.8)		
		4.1 (1.1)	46.8 (12.3)	22 (19.5)	1.5 (0.7)	20.8 (29.7)	3.5 (24.7)	0.02 (0.02)	0.13 (7.1)
	LS	Total (%) = 53.6 (15.7)		Total (%) = 42.4 (53.5)			Total (%) = 2.8 (27.7)		
		6.6 (1.4)	47.0 (14.3)	12.4 (14.2)	3.6 (2.4)	26.4 (36.9)	2.1 (16.5)	0.4 (0.7)	0.2 (10.6)
$MgSiO_3$		Total (%) = 64 (27)		Total (%) = 34 (55)			Total (%) = 0.4 (17)		

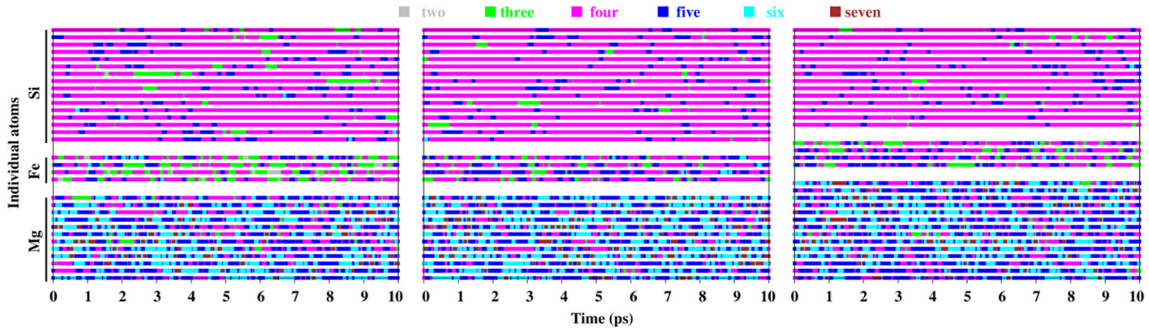

Fig. 7. Temporal cation–anion bonding evolution of Si, Fe and Mg at 3000 K and 0 GPa. *Left:* Fe^{2+} ($Mg_{0.75}Fe_{0.25}SiO_3$); *Middle:* Fe^{3+} ($Mg_{0.75}Fe_{0.25}SiO_{3.125}$); *Right:* Fe^{3+} ($Mg_{0.875}Fe_{0.25}Si_{0.875}O_3$). Cation-anion coordination (two- to seven- fold) numbers are color coded as shown in the legend. (For interpretation of the references to colour in this figure legend, the reader is referred to the web version of this article.)

1991). It is possible that the presence of the larger, lower field strength alkali atoms in these melts facilitates the formation/retention of the tetrahedral Fe^{3+}'s (and BO's), which perhaps help in making alkali-ferrosilicate melts more viscous (Weigel et al., 2006; Giuli et al., 2012; Cicconi et al., 2015). For Fe_2SiO_{4+x} melts, the measured viscosity, however, shows an opposite trend, that is, a decrease in the viscosity with increasing $Fe^{3+}/\Sigma Fe$ ratio (Kaiura et al., 1977), probably indicating compositional dependence of the network forming/modifying ability of Fe^{3+}. Based on our calculated structural results of Fe-bearing $MgSiO_3$ melts and the experimental data on alkali-free ferrosilicate melts/glasses (Alderman et al., 2017a, 2017b), it is likely that the difference in viscosity among the different valence states is not significant.

4.3. Iron-oxygen coordination at equilibrium spin fractions: Fe^{2+} vs. Fe^{3+}

Up until this point, we have discussed the dependence of the structural parameters with pressure and temperature for either fully HS or LS for a given valence state. But, iron in the silicate melts is likely to be in the mixed spin state under mantle conditions. Direct assessment of such mixed spin states is beyond our present capability. However, the spin phase diagrams reported by Karki et al. (2018) provide information about the equilibrium low- and high-spin fractions at high pressure–temperature conditions. It is thus possible to estimate effective structural parameters for those equilibrium mixed spin states and relate them to the mantle conditions. The effective Fe-O coordination-pressure profiles for the stable mixed spin are shown in Fig. 8, and also the influence of iron on the average Si-O and Mg-O coordination is assessed (Fig S2).

Considering the relatively stable mixed spin state, it is apparent that the differences between the ferrous and ferric configurations become significant, particularly at the mid compression range. For instance, along the 3000 K isotherm, the difference in Fe-O coordination between the ferrous and ferric iron reaches to ~0.5, with the ferrous iron displaying an average coordination comparable to the Mg-O value. The spin transition occurs at a relatively higher pressure in Fe^{2+} (Karki et al., 2018). The fraction

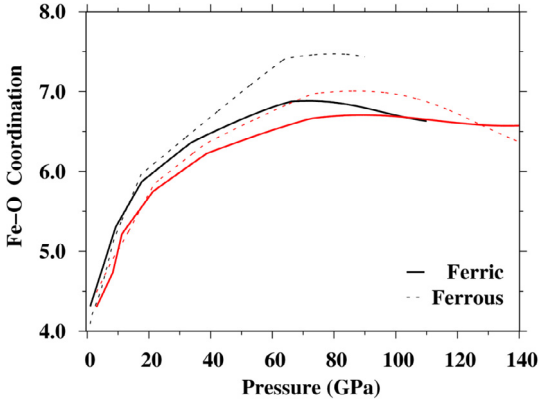

Fig. 8. Pressure profiles of the effective iron-oxygen coordination for mixed spin configurations of ferric (solid curves) and ferrous (dashed curves) iron in silicate melt at 3000 K (black curves) and 4000 K (red curves). The equilibrium fractions of low and high-spin states at different pressure–temperature conditions are extracted from the spin-phase diagrams of Karki et al. (2018). (For interpretation of the references to colour in this figure legend, the reader is referred to the web version of this article.)

of the LS state at any given pressure is thus lower in Fe^{2+} in comparison to Fe^{3+}. For example, around 60 GPa, the proportion of the LS-Fe^{2+} is only 0.03, while the proportion of the LS-Fe^{3+} is 0.13. With most iron remaining in HS in the mid compression range, together with the fact that the average Fe-O coordination in the HS-Fe^{2+} is higher than the HS-Fe^{3+} at those conditions (Fig. 5), the stable Fe^{2+} melt should, therefore, display higher average coordination. At the higher end of the compression, this difference between the Fe^{2+} and Fe^{3+}-bearing stable melts is largely suppressed. Both the melts are thus likely to display similar structural characteristics that originate from the disproportionate abundances of HS and LS in them.

5. SUMMARY

Our FPMD simulations of iron-bearing $MgSiO_3$ melts show that the structural properties associated with iron are more sensitive to its spin state (HS or LS) than to the

valence state (Fe^{2+} or Fe^{3+}). They also predict that for a given spin state, the ferrous iron remains relatively undercoordinated than the ferric iron at low pressures, irrespective of temperature. This is consistent with the experimental inference for MgO–FeO–SiO_2 melts, but the ferrous iron has more neighbor oxygen connections than the ferric iron for many ferrosilicate melts. The ferric–ferrous Fe–O coordination difference persists for the LS state over the entire pressure range considered. The gap between the mean Fe^{2+}–O and Fe^{3+}–O coordination numbers, however, decreases with compression for the HS state without showing a clear trend at high pressures. The atomistic details, such as NBO and BO abundances, and bond breaking/formation activity suggest an equivalent role of the ferrous and ferric iron in terms of their contribution to the structural framework, which is consistent with experimental inference. It has also been reported that the ferrous and ferric iron behave differently in alkali-bearing ferrosilicate melts, with the ferrous iron enhancing and the ferric iron suppressing the melt mobility (decreasing and increasing viscosity, respectively). The atomistic details of such melts from FPMD simulations can help relate the structural properties with the observed viscosity and also possibly unravel the origin of the differences between those melts and Fe-bearing $MgSiO_3$ melts.

Declaration of Competing Interest

The authors declare that they have no known competing financial interests or personal relationships that could have appeared to influence the work reported in this paper.

ACKNOWLEDGMENTS

This work was funded by National Science Foundation (EAR-1764140). High performance computing resources were provided by Louisiana State University (http://www.hpc.lsu.edu) and Louisiana Optical Network Institute (LONI).

APPENDIX A. SUPPLEMENTARY MATERIAL

Supplementary data to this article can be found online at https://doi.org/10.1016/j.gca.2020.03.040.

REFERENCES

Alberto H. V., da Cunha J. L. P., Mysen B. O., Gil J. M. and de Campos N. A. (1996) Analysis of Mössbauer spectra of silicate glasses using a two-dimensional Gaussian distribution of hyperfine parameters. *J. Non-Cryst. Solids* **194**, 48–57.

Alderman O. L. G., Lazareva L., Wilding M. C., Benmore C. J., Heald M., Johnson C. E., Johnson J. A., Hah H. Y., Sendelbach S., Tamalonis A., Skinner L. B., Parise J. B. and Weber J. K. R. (2017a) Local structural variation with oxygen fugacity in Fe_2SiO_{4+x} fayalitic iron silicate melts. *Geochim. Cosmochim. Acta* **203**, 15–36.

Alderman O. L. G., Wilding M. C., Tamalonis A., Sendelbach S., Heald S. M., Benmore C. J., Johnson C. E., Johnson J. A., Hah H. Y. and Weber J. K. R. (2017b) Iron K-edge X-ray absorption near- edge structure spectroscopy of aerodynamically levitated silicate melts and glasses. *Chem. Geol.* **453**, 169–185.

Burkhard D. J. M. (2000) Iron-bearing silicate glasses at ambient conditions. *J. Non-Cryst. Solids* **275**, 175–188.

Cococcioni M. and de Gironcoli S. (2005) Linear response approach to the calculation of the effective interaction parameters in the LDA+U method. *Phys. Rev. B* **71**(3) 035105.

Cicconi M. R., Giuli G., Ertel-Ingrisch W., Paris E. and Dingwell D. B. (2015) The effect of the [Na/(Na + K)] ratio on Fe speciation in phonolitic glasses. *Am. Mineral.* **100**, 1610–1619.

Cochain B., Neuville D. R., Henderson G. S., McCammon C. A., Pinet O. and Richet P. (2012) Effects of the iron content and redox state on the structure of sodium borosilicate glasses: a Raman, Mössbauer and boron k-edge XANES spectroscopy study. *J. Am. Ceram. Soc.* **95**, 962–971.

Dingwell D. B. (1991) Redox viscometry of some Fe-bearing silicate melts. *Am. Mineral.* **76**, 1560–1562.

Dingwell D. B. and Virgo D. (1987) The effect of oxidation-state on the viscosity of melts in the system Na_2O–FeO–Fe_2O_3–SiO_2. *Geochim. Cosmochim. Acta* **51**, 195–205.

Drewitt J. W., Sanloup C., Bytchkov A., Brassamin S. and Hennet L. (2013) Structure of $(Fe_xCa_{1-x}O)_y(SiO_2)_{1-y}$ liquids and glasses from high-energy x-ray diffraction: Implications for the structure of natural basaltic magmas. *Phys. Rev. B* **87** 224201.

Farges F., Lefrere Y., Rossano S., Berthereau A., Calas G. and Brown G. E. (2004) The effect of redox state on the local structural environment of iron in silicate glasses: a molecular dynamics, combined XAFS spectroscopy, and bond valence study. *J. Non-Cryst. Solids* **344**, 176–188.

Ghosh D. B. and Karki B. B. (2016) Solid-liquid density and spin crossovers in (Mg, Fe)O system at deep mantle conditions. *Sci. Rep.* **6**, 37269. https://doi.org/10.1038/srep37269.

Ghosh D. B. and Karki B. B. (2017) Transport properties of carbonated silicate melt at high pressure. *Science Advances.* **3** e1701840.

Giuli G., Alonso-Mori R., Cicconi M. R., Paris E., Glatzel P., Eeckhout S. G. and Scaillet B. (2012) Effect of alkalis on the Fe oxidation state and local environment in peralkaline rhyolitic glasses. *Am. Mineral.* **97**, 468–475.

Guillot B. and Sator N. (2007) A computer simulation study of natural silicate melts. Part I: Low pressure properties. *Geochim. Cosmochim. Acta* **71**, 1249–1265.

Hannoyer B., Lenglet M., Durr J. and Cortes R. (1992) Spectroscopic evidence of octahedral iron(III) in soda-lime silicate glasses. *J. Non-Cryst. Solids* **151**, 209–216.

Henkelman G., Arnaldsson A. and Jónsson H. (2006) A fast and robust algorithm for Bader decomposition of charge density. *Comput. Mater. Sci.* **36**, 354–360.

Holland D., Mekki A., Gee I. A., McConville C. F., Johnson J. A., Johnson C. E., Appleyard P. and Thomas M. (1999) The structure of sodium iron silicate glass: a multi-technique approach. *J. Non-Cryst. Solids* **253**, 192–202.

Holmström E. and Stixrude L. (2015) Spin Crossover in Ferropericlase from First-Principles Molecular Dynamics. *Phys. Rev. Lett.* **114** 117202.

Holmström E. and Stixrude L. (2016) Spin Crossover in liquid (Mg, Fe)O at extreme conditions. *Phys. Rev. B* **93**, 195142.

Jackson W. E., Mustre De Leon J., Brown, Jr, G. E., Waychunas G. A., Conradson S. D. and Combes J.-M. (1993) High-temperature XAS study of Fe_2SiO_4 liquid: Reduced coordination of ferrous iron. *Science* **262**, 229–232.

Jackson W. E., Farges F., Yeager M., Mabrouk P. A., Rossano S., Waychunas G. A., Solomon E. I. and Brown G. E. (2005) Multi-spectroscopic study of Fe(II) in silicate glasses: implications for the coordination environment of Fe(II) in silicate melts. *Geochim. Cosmochim. Acta* **69**, 4315–4332.

Kaiura G., Toguri J. and Marchant G. (1977) Viscosity of fayalite-based slags. *Can. Metall. Quart.* **16**, 156–160.

Karki B. B. (2015) First-principles computation of mantle materials in crystalline and amorphous phases. *Phys. Earth Planet. Inter.* **240**, 43–69.

Karki B. B., Ghosh D. B., Maharjan M., Karato S.-I. and Park J. (2018) Density pressure profiles of Fe bearing $MgSiO_3$ liquid: Effects of valence and spin states, and implications for the chemical evolution of the lower mantle. *Geophys. Res. Lett.*. https://doi.org/10.1029/2018GL077149.

Kim H.-I., Sur J. C. and Lee S. K. (2016) Effect of iron content on the structure and disorder of iron- bearing sodium silicate glasses: A high-resolution ^{29}Si and ^{17}O solid-state NMR study. *Geochim. Cosmochim. Acta* **173**, 160–180.

Kim H.-I. and Lee S. K. (2019) The degree of polymerization and structural disorder in (Mg, Fe)SiO_3 glasses and melts: Insights from high-resolution ^{29}Si and ^{17}O solid-state NMR. *Geochim. Cosmochim. Acta* **250**, 268–291.

Koch D., Golub P. and Manzhou S. (2018) Stability of charges in titanium compounds and charge transfer to oxygen in titanium dioxide. *J. Phys.: Conf. Series* **1136**, 012017.

Kresse G. and Furthmüller J. (1996) Efficient iterative schemes for ab initio total-energy calculations using a plane-wave basis set. *Phys. Rev. B* **54**, 11169–11186.

Kukkadapu R.K., Li H., Smith G.L., Crum J.D., Jeoung J.S., Poisl W.H., Weinberg M.C. (2003) Mössbauer and optical spectroscopic study of temperature and redox effects on iron local environments in a Fe-doped (0.5 mol% Fe_2O_3) $18Na_2O$–$72SiO_2$ glass, J. Non-Cryst. Solids 317, 301-318.

Lange, R. A. and Carmichael, I. S. E., (1990) Thermodynamic properties of silicate liquids with emphasis on density, thermal expansion and compressibility. In J. Nicholls and J.K. Russell, Eds., Modern methods of igneous petrology: Understanding magmatic processes, 24, p. 25–64. Reviews in Mineralogy, Mineralogical Society of America, Chantilly, Virginia.

Liu Q. and Lange R. A. (2006) The partial molar volume of Fe_2O_3 in alkali silicate melts: Evidence for an average Fe^{3+} coordination number near five. *Am. Mineral.* **91**, 385–393.

Mysen B. O. (2006) The structural behavior of ferric and ferrous iron in aluminosilicate glass near meta-aluminosilicate joins. *Geochim. Cosmochim. Acta* **70**, 2337–2353.

Mysen B. O., Seifert F. and Virgo D. (1980) Structure and redox equilibria of iron-bearing silicate melts. *Am. Mineral.* **65**, 867–884.

Mysen B. O., Virgo D., Neumann E. R. and Seifert F. A. (1985) Redox equilibria and the structural states of ferric and ferrous iron in melts in the system CaO–MgO–Al_2O_3–SiO_2–Fe–O: relationships between redox equilibria, melt structure and liquidus phase-equilibria. *Am. Mineral.* **70**, 317–331.

Mysen B. O. and Virgo D. (1989) Redox equilibria, structure, and properties of Fe-bearing aluminosilicate melts: relationships among temperature, composition, and oxygen fugacity in the system Na_2O–Al_2O_3–SiO_2–Fe–O. *Am. Mineral.* **74**, 58–76.

Nosé S. (1984) A unified formulation of the constant temperature molecular dynamics methods. *J. Chem. Phys.* **81**(1), 511–519.

Ramo D. M. and Stixrude L. (2014) Spin crossover in Fe_2SiO_4 liquid at high pressure. *Geophys. Res. Lett.* **41**, 4512–4518.

Rollmann G., Rohrbach A., Entel P. and Hafner J. (2004) First-principles calculation of the structure and magnetic phases of hematite. *Phys. Rev. B* **69**, 165107.

Rossano S., Ramos A., Delaye J. M., Creux S., Filipponi A., Brouder C. and Calas G. (2000) EXAFS and Molecular Dynamics combined study of CaO–FeO–$2SiO_2$ glass: new insight into site significance in silicate glasses. *Europhys. Lett.* **49**, 597–602.

Sanson A., Kantor I., Cerantola V., Irifune T., Carnera A. and Pascarelli S. (2016) Local structure and spin transition in Fe_2O_3 hematite at high pressure. *Phys. Rev. B* **94**, 014112.

Stevenson D. J. (1989) Formation and early evolution of the Earth. In Mantle Convection: Plate Tectonics and Global Dynamics (ed.W. R. Peltier). Gordon and Breach, New York, pp. 817–873.

Sun Y., Zhou H., Yin K., Zhao M., Xu S. and Lu X. (2018) Transport properties of Fe_2SiO_4 melt at high pressure from classical molecular dynamics: Implications for the lifetime of the magma ocean. *J. Geophys. Res.*. https://doi.org/10.1029/2018JB015452.

Sun Y., Zhou H., Yin K. and Lu X. (2019) First principles study of thermodynamics and spin transition in $FeSiO_3$ liquid at high pressure. *Geophys. Res. Lett.* **46**, 3706–3716.

Tang W., Sanville E. and Henkelman G., A grid-based Bader analysis algorithm without lattice bias, J. Phys. Condens. Matter, 21, 2009, 084204.

Toplis M. J. and Carroll M. R. (1995) An experimental study of the influence of oxygen fugacity on Fe–Ti oxide stability, phase relations, and mineral-melt equilibria in ferro-basaltic systems. Journal of Petrology, 36, 1137–1170.

Wang B., Shaohong L., Li L. and Truhlar D. G. (2014) Modeling the partial atomic charges in inorganometallic molecules and solids and charge redistribution in Lithium-ion cathodes. *J. Chem. Theory Comput.* **10**, 5640–5650.

Waychunas G. A., Brown G. E., Ponader C. W. and Jackson W. E. (1988) Evidence from X-ray absorption for network-forming Fe^{2+} in molten alkali silicates. *Nature* **332**, 251–253.

Weigel C., Cormier L., Galoisy L., Calas G., Bowron D. and Beuneu B. (2006) Determination of Fe^{3+} sites in a $NaFeSi_2O_6$ glass by neutron diffraction with isotopic substitution coupled with numerical simulation. *Appl. Phys. Lett.* **89** 141911.

Wilke M., Partzsch G. M., Bernhardt R. and Lattard D. (2004) Determination of the iron oxidation state in basaltic glasses using XANES at the K-edge. *Chem. Geol.* **213**, 71–87.

Wilke M., Farges F., Partzsch G. M., Schmidt C. and Behrens H. (2007) Speciation of Fe in silicate glasses and melts by in-situ XANES spectroscopy. *Am. Mineral.* **92**, 44–56.

Zhang H. L., Hirschmann M. M., Cottrell E., Newville M. and Lanzirotti A. (2016) Structural environment of iron and accurate determination of Fe^{3+}/ ΣFe ratios in andesitic glasses by XANES and Mössbauer spectroscopy. *Chem. Geo.* **428**, 48–58.

Associate editor: James Van Orman